Measurement Report: Elevated atmospheric ammonia may promote the particle pH and HONO formation: Insights from the COVID-19 pandemic

Xinyuan Zhang[1,2], Lingling Wang[3], Nan Wang[3], Shuangliang Ma[3], Shenbo Wang[2,4 *], Ruiqin Zhang[2,4**], Dong Zhang[1,2], Mingkai Wang[2,4], Hongyu Zhang[1,2].

[1] College of Chemistry, Zhengzhou University, Zhengzhou, 450000, China

[2] Research Institute of Environmental Sciences, Zhengzhou University, Zhengzhou 450000, China

[3] Henan Provincial Ecological Environment Monitoring and Safety Center, Zhengzhou, 450000, China

[4] School of Ecology and Environment, Zhengzhou University, Zhengzhou, 450000, China

Correspondence: Shenbo Wang (shbwang@zzu.edu.cn) and Ruiqin Zhang (rqzhang@zzu.edu.cn)

Abstract

HONO plays a crucial role as a precursor to OH radicals in the tropospheric atmosphere. The incongruity between HONO concentration and NO_x emissions during the COVID-19 pandemic remains puzzling. Here, we show evidence from field observations of ten sites in China that there was a noticeable increase in NH_3 concentrations during the COVID-19 pandemic. In addition to the meteorological conditions, the significant decrease in sulfate and nitrate concentrations enhanced the portioning of NH_4^+ to NH_3. Sensitivity analysis indicated that the decrease in anion concentrations (especially sulfate and nitrate) and the increase in cation concentrations during the COVID-19 pandemic led to an increase in particle pH. In other words, changes in the excess ammonia drove changes in particle pH that may consequently have impacted the rate of HONO formation. The calculation of reaction rates indicates that during the epidemic, the increase in pH may promote the generation of HONO by facilitating redox reactions, which highlights the importance of coordinating the control of SO_2, NO_x, and NH_3 emissions.

Keywords: Ammonia, HONO, Gas-particle portioning, Acidity, COVID-19 pandemic

1. Introduction

Nitrous acid (HONO) is a critical precursor of hydroxyl radical (OH), contributing to more than 60% of OH production (Alicke, 2003;Platt et al., 1980;Kleffmann et al., 2005). The OH can react with carbon monoxide, nitrogen oxides (NO_x), sulfur dioxide (SO_2), and volatile organic compounds to produce secondary pollutants such as ozone (O_3) and $PM_{2.5}$ (particulate matter with an aerodynamic diameter less than or equal to 2.5 μm), thereby affecting air quality, human health, and global climate change (Li et al., 2021a;Wang et al., 2023b;Lu et al., 2018)

High concentrations of HONO are present in urban daytime atmospheres, and exploring its sources has become a hot and challenging topic in the field of atmospheric chemistry (Jiang et al., 2022;Xu et al., 2019). Various sources of atmospheric HONO have been identified, including combustion processes (e.g., vehicle emissions) (Kramer et al., 2020;Liao et al., 2021a;Li et al., 2021b), direct emissions from soil (Su and Zhang, 2011;Oswald et al., 2013;Meusel et al., 2018), homogeneous reactions between NO and OH radicals (Pagsberg, 1997;Atkinson and Rossi, 2004), heterogeneous reactions of NO_2 on aerosols and ground surfaces (Zhang et al., 2020a;McFall et al., 2018;Liu et al., 2014;Liu et al., 2020a), and photolysis of nitrate (Spataro and Ianniello, 2014;Scharko et al., 2014;Romer et al., 2018;Ye et al., 2017;Shi et al., 2021). During the pandemic control periods, there was a substantial reduction in vehicle traffic flow and industrial emissions, leading to a decrease of more than 60% in NO_x emissions in eastern China (Huang et al., 2021a). It was initially expected that the concentration of HONO would also decrease proportionally. However, Liu et al. (2020b) observed that the decrease in

HONO concentration during the pandemic period was only 31% (from 1.5 ppb to 0.9 ppb), which was significantly lower than the reductions in NO (62%, from 26.3 to 4.2 ppb) and NO_2 (36%, from 15.5 to 6.2 ppb). Furthermore, the observed concentrations of HONO during the COVID-19 pandemic in 2020 were higher than those during the corresponding period in 2021 in Beijing (Luo et al., 2023). These findings suggest the existence of a considerable unknown source of HONO during the COVID-19 pandemic period.

Ammonia (NH_3) is a primary alkaline gas in the atmosphere, capable of influencing the pH level of particulate matter and plays a crucial role in the atmospheric nitrogen cycle (Gu et al., 2022;Xu et al., 2020;Gong et al., 2011). Several studies have indicated that NH_3 can promote the formation of HONO by promoting the hydrolysis of NO_2 (Xu et al., 2019) or the redox reaction of NO_2 with SO_2 (Liu et al., 2023). Moreover, previous studies have reported that NH_3 concentrations in the atmosphere, particularly in rural areas, significantly increased during the pandemic (Xu et al., 2022). Consequently, the rise in NH_3 may contribute to the enhanced formation of HONO (Huang et al., 2021a). Unfortunately, there is currently a lack of research on the relationship between enhanced NH_3 and HONO during the COVID-19 pandemic period.

To address this, online observational data on the chemical composition of $PM_{2.5}$, gaseous pollutants, and meteorological conditions at ten sites in China before and during the COVID-19 pandemic period were analyzed to investigate the variation in NH_3 concentrations and particle pH, and explore the promoting effect of increased pH values on HONO formation.

2. Materials and methods

2.1 Observation sites

Online measurements were conducted at four urban and six rural sites in Henan Province, China from January 1 to February 29, 2020, including Sanmenxia (U-SMX), Zhoukou (U-ZK), Zhumadian (U-ZMD), and Xinyang (U-XY), as well as rural locations including Anyang (R-AY), Xinxiang (R-XX), Jiaozuo (R-JZ), Shangqiu (R-SQ), Nanyang (R-NY), and Puyang (R-PY). Descriptions and the spatial distribution of these ten sites can be found in Table S1 and Fig. S1.

2.2 Measurements

The aerosol and gas monitor (MARGA, Metrohm, Switzerland) was used to analyze the hourly water-soluble ions (Na^+, NH_4^+, K^+, Mg^{2+}, Ca^{2+}, Cl^-, NO_3^-, and SO_4^{2-}) in $PM_{2.5}$, as well as gaseous species (NH_3, HNO_3, HCl, and HONO) at ten sampling sites. The MARGA instrument is widely used (Chen et al., 2017;Stieger et al., 2019;Twigg et al., 2022). A detailed description of the instrument and QA/QC can be found in Text S1. In brief, the atmospheric sample passes through a $PM_{2.5}$ cut-off head, and both particles and gases enter a wet rotating dissolution device for diffusion. Subsequently, the particles in the sample undergo hygroscopic growth and condensation in an aerosol supersaturated vapor generator, followed by collection and ion chromatographic analysis. The gases in the sample are oxidized by H_2O_2 in the dissolution device, absorbed into a liquid solvent, and then entered the gas sample collection chamber for

ion chromatographic quantification. The range of minimum detection limits for water-soluble ions was between 0.002 μg/m^3 (Cl^-) to 0.081 μg/m^3 (NH_4^+). Uncertainties of 20% are assumed for the detection of NH_3 and NH_4^+, while uncertainties of 10% are assumed for other components (Wang et al., 2020;Wang et al., 2022). In addition, a detailed description of HONO measurement using this system can be found in Text S2. Overall, the limit of detection for HONO was 4 pptv and the uncertainty was estimated to be ± 20%.

The data for NO_2 and SO_2 were obtained from a series of instruments provided by Thermo Fisher Scientific (USA). The hourly concentrations of organic carbon (OC) in $PM_{2.5}$ were analyzed using a carbon analyzer (Model 4, Sunset Laboratory., USA). Detailed descriptions of the NO_2, SO_2, and carbon analyzers can be found in Text S3. The smart weather stations (LUFFTWS500, Sutron, Germany) were utilized for synchronized observation of meteorological parameters including pressure, temperature (T), and relative humidity (RH).

2.3 Data analysis.

2.3.1 pH prediction.

The thermodynamic model ISORROPIA-II was used to estimate the pH value of the particles (Fountoukis, 2007) by inputting RH, T, K^+, Ca^{2+}, Mg^{2+}, total ammonia ($TNH_x = 17 \times (\frac{[NH_4^+]}{18} + \frac{[NH_3]}{17})$), total sulfuric acid ($TH_2SO_4$, SO_4^{2-}), total sodium (TNa, Na^+), total chlorine (TCl, Cl^-), and total nitrate ($TNO_3 = NO_3^- + HNO_3$). The

model has two calculation modes: the forward mode and reverse mode, and the aerosol dissolution systems can be set to simulate a metastable state (aqueous phase) or stable state (aqueous and solid phase). Studies have shown that the forward mode is less affected by instrument measurement errors than the reverse mode (Ding et al., 2019;Song et al., 2018). Additionally, the minimum average RH of about 55% was recorded during the sampling period at the ten sites. Thus, ISORROPIA-II was run in the forward model for the aerosol system in the metastable condition and only used data with RH ≥ 30% for simulation accuracy (Ding et al., 2019;Song et al., 2018). The ISORROPIA model calculated the particle hydrate ion concentration per volume of air (H_{air}^{+}) and aerosol water associated with inorganic matter (AWC_{inorg}). The pH value was calculated using the following equation (Bougiatioti et al., 2016):

$$pH = -\log_{10}H_{aq}^{+} = -\log_{10}\frac{1000H_{air}^{+}}{AWC_{inorg} + AWC_{org}} \quad (2.1)$$

where the modeled concentrations for AWC_{inorg} and H_{air}^{+} are μg/m^3, and AWC_{org} is the particle water associated with the organic matters predicted using the following method:

$$AWC_{org} = \frac{m_s}{\rho_s}\frac{k_{org}}{\left(\frac{1}{RH} - 1\right)} \quad (2.2)$$

where m_s is the mass concentration of organic matter (OM = OC × f). The f is the conversion factor of OC, which is dependent on the extent of OM oxidation and secondary organic aerosol formation (Chow et al., 2015). Studies on the ratio of OM/OC in fourteen cities in China suggested that the mean value of f was 1.59 ± 0.18 during the winter season in Northern China (Xing et al., 2013), and thus we adopted 1.6 as the f in this study. k_{org} is the organic hygroscopicity parameter and depends on organic

functionality, water solubility, molecular weight, and oxidation level. Han et al. (2022) have reported that the k_{org} generally increased with O: C ratios, with a range of 0–0.3 for 23 organics, including carboxylic acids, amino acids, sugars, and alcohols. Gunthe et al. (2011) estimated a $k_{org} = 0.06 \pm 0.01$ for the effective average hygroscopicity of the non-refractory organic particulate matter in the aerosols in Beijing. Our previous study has estimated that the uncertainties of k_{org} value (0.06) for pH in the range of 0–0.3 only lead to –1–3% errors, which can be neglected (Wang et al., 2023a). Therefore, the value of 0.06 was selected in this paper. ρ_s is the organic density, which was chosen to be 1.35 g/cm^3 following previous studies (Table S2).

2.3.2 The sources of HONO

The sources of HONO include direct emission (P_{emi}), the homogeneous reaction of NO and •OH (P_{OH+NO}), the heterogeneous reaction of NO_2 on the ground (P_{ground}) and aerosol ($P_{aerosol}$), the photo-enhanced heterogeneous reaction of NO_2 on the ground ($P_{ground+hv}$) and aerosol ($P_{aerosol+hv}$), and nitrate photolysis ($P_{nitrate}$). The detailed calculation method is described in the Supplementary Material (Text S4, Table S3, Figs. S2 and S3).

Soil emission has been demonstrated to be a major source of HONO, which is affected by temperature to some extent (Liu et al., 2020c;Liu et al., 2020b). However, during the sampling periods, there was no significant positive correlation between HONO concentration and temperature (Fig. S4). In addition, temperatures did not exceed 10°C, under which the soil HONO emission rate is generally considered to be zero (Zhang et

al., 2023). Furthermore, the equilibrium gas-phase concentration over an aqueous solution of nitrous acid, [HONO]*, a key parameter controlling the exchange of HONO between the gas and aqueous phase in soil, is calculated according to Su et al.(2011). The results indicate that the temperature difference between PC and DC periods only led to approximately a 0.01% concentration change. On the other hand, studies on the sources of HONO in the North China Plain of China during winter consistently showed that soil HONO emissions contribute around 1% (Liu et al., 2020c;Liu et al., 2020b;Zhang et al., 2023). Therefore, this study does not consider soil HONO emissions.

2.3.3 Redox reaction of NO_2 with SO_2.

The redox reaction of NO_2 with SO_2 (R_1) is considered a crucial potential source of high concentrations of HONO in Northern China (Cheng et al., 2019;Wang et al., 2016):

$$S(IV) + 2NO_2 + H_2O \rightarrow S(VI) + 2H^+ + 2NO_2^- \quad (R_1)$$

the rate expression for reaction (R_1) was estimated to:

$$d[S(VI)] / dt = k_1[NO_2][S(VI)], \quad (2.3)$$

the rate constant k_1 value is pH dependent, e.g., for pH, 5, $k_1 = (1.4\times10^5+1.24\times10^7)/2$ M^{-1} s^{-1}. For k_1 values under other pH conditions and other related information, please refer to Text S5, Table S4, and Table S5.

3. Results and discussion

3.1 Variations of NH_3, NH_4^+ and TNH_x.

The temporal variations of NH_3, NH_4^+, and TNH_x at 10 sampling sites in the pre-COVID-19 pandemic period (PC, January 1 to 23, 2020) and during the COVID-19 pandemic period (DC, January 24 to February 29, 2020) are presented in Fig. 1, with their average concentration listed in Table 1. In general, rural sites exhibited higher concentrations of NH_3, NH_4^+, and TNH_x compared to urban sites, except for the R-NY site. This finding is consistent with previous studies conducted in Zhengzhou (Wang et al., 2020), Shanghai (Chang et al., 2019), and Quzhou (Feng et al., 2022), owing to the intense agricultural ammonia emissions. The highest concentrations of NH_3 and TNH_x were recorded at site R-JZ, with average values of 25.3 ± 11.5 and 40.8 ± 20.1 μg/m^3, respectively. Site R-AY had the highest NH_4^+ concentration, measuring 19.3 ± 12.9 μg/m^3. Note that the current study area exhibited higher NH_3 levels compared to other regions (Table S6), which probably was attributed to the highest NH_3 emissions of Henan Province in China, primarily from nitrogen fertilizer application and livestock farming (Wang et al., 2018;Ma, 2020).

Compared to the PC, NH_3 concentrations increased in the DC at all sites. Notably, rural sites experienced more significant increases in NH_3 concentrations than urban sites, which was similar to the trend in Shanghai (Xu et al., 2022). The largest increases in NH_3 concentrations were observed at R-SQ (71%, 7.3 μg/m^3) and U-ZK (37%, 4.8 μg/m^3) for rural and urban sites, respectively. In contrast, the concentrations of NH_4^+

and TNH_x decreased in the DC with the largest reduction at rural site R-PY (51%, 12.9 μg/m^3) and urban site U-ZMD (48%, 9.3 μg/m^3). Regarding TNH_x, rural sites exhibited larger reductions, with site R-SQ experiencing the largest decrease of 37% (4.7 μg/m^3).

Figure 2 illustrates the spatial distribution and the diurnal variation of NH_3 concentrations at the ten sites before and during the pandemic. NH_3 concentrations in most sites exhibited an unimodal trend in PC that NH_3 concentrations gradually increased after sunrise, reaching a peak around noon (11:00–12:00), and then decreased to a valley around 16:00–17:00. This diurnal pattern is similar to NH_3 variations observed in urban areas of Houston, USA, as a result of the natural emissions from vegetation and soil during photosynthesis (Gong et al., 2011). However, other studies have recorded a significant NH_3 peak during the early morning of 8:00–10:00 (Ellis et al., 2011;Meng et al., 2018;Gu et al., 2022), suggesting the influence of vehicle emissions (Gong et al., 2011;Gu et al., 2022), residual NH_3 mixing, soil or plant emissions (Ellis et al., 2011), and dew volatilization (Wentworth et al., 2016;Huang et al., 2021b). Therefore, the NH_3 in urban and rural areas of this study was probably less affected by NH_3 emissions from vehicles, different from the recent studies in megacities of China (e.g., Beijing and Shanghai) (Gu et al., 2022;Wu et al., 2023;Zhang et al., 2020b). In addition to the transport from agricultural emissions, urban NH_3 in this region might also originate from other non-agricultural sources, such as wastewater treatment, coal combustion, household waste, urban green spaces, and human excrement (Chang et al., 2019).

During the COVID-19 pandemic, the diurnal variation of NH_3 in both urban and rural

sites still maintained an unimodal distribution. The peak values in urban sites remained consistent with PC levels, further demonstrating that the influence of vehicles on NH_3 in urban areas was limited. Notably, the peak time of NH_3 in rural sites shifted 1–2 hours earlier compared to the trend in PC. Ammonia in rural areas primarily originates from nitrogen fertilizer application, livestock, and poultry breeding (Feng et al., 2022;Meng et al., 2018), which are significantly influenced by T and RH (Liu et al., 2023). Table S7 and Fig. S5 reveal that there was an increased T and a decreased RH at rural sites in the DC than the PC, which could accelerate the evaporation of NH_3 and thus potentially lead to earlier peak NH_3 concentrations.

3.2 Gas-to-particle conversion of NH_3

The increased NH_3 accompanying decreased NH_4^+ in the DC suggests that the gas-particle partition of NH_3/ NH_4^+ may determine the elevated NH_3 concentrations. Meteorological parameters, including RH and T, play a crucial role in the gas-particle partitioning of NH_3 (Liu et al., 2023;Xu et al., 2020). Therefore, the higher T and lower RH in the DC (Table S7 and Fig. S5) favored the conversion of NH_4^+ to NH_3, resulting in a decrease in $\varepsilon(NH_4^+)$ ($[NH_4^+]/([NH_3] + [NH_4^+])$ compared to those in the PC (Table S7).

NH_3 primarily enters particles to neutralize acidic ions (Wang et al., 2020;Xu et al., 2020;Liu et al., 2017;Ye et al., 2011;Wells, 1998). Accordingly, the concentrations of required ammonia (Required-NH_x) and excess ammonia (Excess-NH_x) were calculated based on the acidic substances as follows (Wang et al., 2020):

$$\text{Required-NH}_x = 17 \times \left(\frac{[SO_4^{2-}]}{48} + \frac{[NO_3^-]}{63} + \frac{[Cl^-]}{35.5} + \frac{[HNO_3]}{64} + \frac{[HCl]}{36.5}\right) - 17 \times \left(\frac{[Na^+]}{23} + \frac{[K^+]}{39} + \frac{[Ca^{2+}]}{20} + \frac{[Mg^{2+}]}{12}\right) \quad (3.1)$$

$$\text{Excess-NH}_x = \text{TNH}_x - \text{Required-NH}_x \quad (3.2)$$

where [W] represents the concentration of the substance (μg/m^3). The significant linear fitting (R^2 is greater than 0.96, and the slope is close to 1) in Fig. S6 demonstrates that the anions and cations at each site were close to the equilibrium state. Therefore, the organic acids in $PM_{2.5}$ may have less effect on NH_3 and NH_4^+ and were not considered in Formula 3.1.

As shown in Fig. 3 and Table S8, compared to those in the PC, the concentration of Required-NH_x in the DC significantly decreased (ranging from 37% at site R-JZ to 58% at site R-PY), while the concentration of Excess-NH_x increased (ranging from 9% at site R-AY to 78% at site R-SQ). The reduction in the concentrations of sulfate and nitrate (Fig. S7) was responsible for the decrease in the concentration of Required-NH_x. To sum up, in addition to meteorological conditions, the substantial reduction in anthropogenic emissions of SO_2, NO_x, and other pollutants in the DC had led to a decrease in acidic substances (e.g., sulfate and nitrate) in particles, in turn, resulting in more gas-phase NH_3 concentration remaining in the atmosphere.

3.3 Particle pH before and during COVID-19

Diurnal patterns of particle pH in PC and DC at ten sites are summarized in Fig. 4 with their average values listed in Table S9. $PM_{2.5}$ shows consistent moderate acidity, with mean values in the range of 4.2–5.1, which were close to the values in previous

studies (Table S9). Compared to the PC, the particle pH at ten sites increased obviously in the DC, with the highest increase of 0.5 (U-ZK) and 0.3 (R-PY) at urban and rural sites, respectively, which were the subject of an in-depth discussion in the following text.

To explore the dominant factors that determine the local particle pH level and result in the high pH during the DC, sensitivity tests of pH to chemical species (i.e., TNH_x, TH_2SO_4, TNO_3, TCl, TNa, K^+, Ca^{2+}, and Mg^{2+}) and meteorological parameters (i.e., T and RH) were performed. A given range for a variable (i.e., TNH_x) with corresponding average values of other parameters (i.e., TH_2SO_4, TNO_3, TCl, TNa, K^+, Ca^{2+}, Mg^{2+}, T, and RH) was input into the model and simulated to compare its effects on pH. As shown in Fig. S8, pH increases with the cation concentrations (i.e., TNH_x, Na^+, K^+, Ca^{2+}, and Mg^{2+}) increasing as well as the anion concentrations (i.e., TH_2SO_4, TNO_3, and Cl^-), T and RH decreasing. According to the average values of input data during PC (Blue line in Fig. S8) and DC (Red line in Fig. S8) at U-ZK and R-PY sites respectively, the changes in pH (ΔpH in Fig. 5) indicate that the decrease in TNH_x concentration and the increase in T in DC led to a decrease in pH values (ΔpH: 0.09 at U-ZK and 0.08 at R-PY sites) compared to PC. However, this effect was outweighed by the decrease in TH_2SO_4 (ΔpH: 0.07 and 0.8 at U-ZK and R-PY sites, respectively) and TNO_3 (ΔpH: 0.05 and 0.4 at U-ZK and R-PY sites, respectively) concentrations as well as the increase in K^+ (ΔpH: 0.03 at U-ZK and 0.2 at R-PY site) and Mg^{2+} (ΔpH: 0.01 at U-ZK and 0.04 at R-PY site) concentrations in the DC, and resulting in an overall increase in pH values in the DC. Furthermore, the relationship between particle pH with the

concentrations of Required-NH_x, and Excess-NH_x, which considers all chemical components, is investigated to examine the dominant factor on the increasing pH in DC. As shown in Fig. 6, the higher Excess-NH_x concentrations in the DC led to higher increases in pH values (ΔpH: 1 at U-ZK and 0.5 at R-PY site) than those in PC (ΔpH: 0.3 at U-ZK and 0.2 at R-PY site), thus Excess-NH_x concentrations may be the key factor in promoting the pH values.

3.4 The influence of pH on HONO.

The observed HONO concentrations decreased by 18% and 54% at U-ZK (0.8 ppb) and R-PY (0.9 ppb) sites in the DC, respectively, compared to those (1.0 and 2.2 ppb) in the PC. Moreover, all the known HONO production sources rates including P_{emi}, P_{OH+NO}, P_{ground}, $P_{ground+hv}$, $P_{aerosol}$, $P_{aerosol+hv}$, and $P_{nitrate}$ (Fig. 7, Fig S9 and S10) show a decreasing trend from PC to DC, with the total reductions of 38% (from 30% to 45% in the scenario with the minimum and maximum uncertainty, respectively) and 79% (from 77% to 82% in the scenario with the minimum and maximum uncertainty, respectively) for U-ZK and R-PY, respectively. At the U-ZK, $P_{ground+hv}$ decreased the most (84%), while at the R-PY, $P_{nitrate}$ had the largest decrease about 85%, which was speculated to be related to the decrease of NO_x and NO_3^- concentration in DC. Note that the reduction rates in the overall known source and almost individual sources were greater than the reduction rates in HONO concentrations (Figs. 7 and 8), thus we hypothesized that there should be other sources capable of promoting HONO production.

There were positive correlations between HONO with SO_2, Excess-NH_x, SO_4^{2-}, and pH (Fig. S12) indicating that the R_1 reaction might form an amount of HONO and contribute to less reduction in the observed HONO concentrations. Considering that R_1 mainly reacts in the liquid phase, the calculated reaction rates of R_1 under the conditions

311 of RH > 60% in the PC and DC periods are illustrated in Figs. 8 and S12. Despite the
312 decrease in NO_2 and SO_2 concentrations in the DC, the increase in particle pH,
313 increasing HSO_3^- concentration in the aqueous phase, promoted the R_1 reaction rates by
314 58% and 59% at U-ZK and R-PY (Figure 8), respectively. Consequently, the enhanced
315 R_1 reaction might prevent a large decrease in HONO (18% at U-ZK and 53% at R-PY)
316 under the conditions of a significant reduction in vehicle emissions and a decline of 66%
317 and 69% in NO_2 concentrations at U-ZK and R-PY, respectively.

318 ## 3.5 Uncertainty

319 According to sensitivity tests of pH (Fig. S8) and R_1 (Fig. S12), pH increases with
320 the concentrations of cations (TNH_x, TNa, K^+, Ca^{2+}, and Mg^{2+}) and OC increasing as
321 well as anions (TH_2SO_4, TNO_3, and Cl^-) concentrations, T, and RH decreasing. R_1
322 reaction rate increases with the concentrations of AWC, NO_2, SO_2, pH, and pressure,
323 while increasing as well as T decreasing. Therefore, two extreme scenarios (i.e., the
324 maximum and minimum rate scenarios) were evaluated to estimate the uncertainty of
325 pH, and R_1 based on the measurement uncertainties at the U-ZK and R-PY sites. Figure
326 S13 suggests that the two extreme scenarios can lead to –10–7% and –71–125%
327 uncertainties at the U-ZK site and –10–7% and –78–123% uncertainties at the R-PY
328 site for pH and R_1, respectively. Even considering the above uncertainty in Fig. 8, it can
329 still be observed that during the DC period, the decrease in HONO was less than that
330 of NO_2, and the rate of the R_1 reaction increased.

331 Considering the conclusions of this study are based solely on observational data,

there are certain limitations. For example, only the changes in the R_1 reaction of $PM_{2.5}$ were calculated, without considering variations in components, pH values, and R_1 reaction rates of coarse particles. Additionally, although this study selected scenarios with RH > 60% to calculate the R_1 reaction to ensure the presence of a liquid phase, it is evident that this approach overlooks some R_1 reactions. Furthermore, due to thermodynamic model calculations of pH values, changes in the mixed state of particle components, and the omission of organic acids, alongside the absence of gaseous HNO_3 and HCl in this study, these factors may lead to inaccuracies in pH value simulations and uncertainty in R_1 calculations(Pye et al., 2020;Haskins et al., 2018;Nah et al., 2018). Therefore, there is a certain degree of uncertainty in the conclusions regarding the growth of R_1 reactions in this paper. Nevertheless, by calculating the changes in R_1 reactions, this study provides a possible explanation for the relatively small decrease in HONO during the epidemic period.

4. Conclusions

Elevated NH_3 concentration was observed during the COVID-19 pandemic at both urban and rural sites in China. In addition to the rise in T and decrease in RH during the COVID-19 pandemic, which favored the conversion of NH_4^+ to NH_3, the significant decrease in sulfate and nitrate concentrations led to the decline in Required-NH_x and was beneficial to the particle-phase NH_4^+ portioning to gas-phase NH_3. Furthermore, under the environmental conditions of increased anion concentrations (especially sulfate and nitrate) and increased cation concentrations, the pH values increased by 0.5

and 0.3 at U-ZK and R-PY sites increased during the pandemic, respectively. Consequently, the high pH values accelerated the formation rate of HONO through the oxidation-reduction reaction of NO_2 with SO_2 (an increase of 58% at U-ZK and 59% at R-PY, respectively), partially compensating for the decrease in HONO concentration caused by the decline in vehicle emissions, NO_2 and NO_3^- concentrations during the COVID-19 pandemic.

5. Implications

HONO plays a crucial role as a precursor to OH radicals in the tropospheric atmosphere (Xue, 2022). There have been significant observations of high HONO concentrations in urban areas during the daytime, leading to a growing interest in understanding its sources in atmospheric chemistry (Jiang et al., 2022;Xu et al., 2019). The heterogeneous reaction mechanism of NO_2 on aerosol surfaces is currently the focus of research on HONO sources, particularly in regions with elevated levels of atmospheric particulate matter, where it could potentially become a major contributor to HONO production (Zhang et al., 2022;Liao et al., 2021b). One of the pathways for heterogeneous reactions on aerosol surfaces is the redox reaction of NO_2 with SO_2. However, the significance of this reaction in HONO production in the real atmosphere is often overlooked, as it relies on the high pH of aerosols (Ge et al., 2019). In recent years, there has been increasing attention on the enhancing effect of NH_3 on the redox reaction, with laboratory experiments demonstrating its ability to generate substantial amounts of HONO (Ge et al., 2019). This study highlights the importance of this

reaction based on actual atmospheric observations. Furthermore, numerous studies have indicated that if control over NH_3 emissions continues to relax while SO_2 and NO_2 emissions decrease, the particle pH in future China is expected to rise steadily (Xie et al., 2020;Song et al., 2019;Wang et al., 2020). Consequently, the redox reaction of NO_2 with SO_2 could become a significant source of HONO in China. Therefore, it is crucial to coordinate the control of SO_2, NO_x, and NH_3 emissions to avoid a rapid increase in the particle pH.

Data availability: All the data presented in this article can be accessed through https://zenodo.org/records/10273539. (Zhang, 2023).

Author contributions. XZ Data Curation, Writing - Original Draft, Visualization. LW, NW, SM, and DZ Investigation, Visualization, Data Curation. DZ, HZ, and MW Investigation. SW Conceptualization, Data Curation, Supervision. RZ Data Curation, Funding acquisition. All people are involved in the discussion of the results.

Competing interest. The authors declare no competing financial interest.

Acknowledgments. This work was supported by the China Postdoctoral Science Foundation (2023M733220), the Zhengzhou $PM_{2.5}$ and O_3 Collaborative Control and Monitoring Project (20220347A), and the National Key Research and Development Program of China (No. 2017YFC0212403).

References

Alicke, B.: OH formation by HONO photolysis during the BERLIOZ experiment, J. Geophy. Res., 108, 8247, https://doi.org/10.1029/2001JD000579, 2003.

Atkinson, R., Baulch, D.L., Cox, R.A., Crowley, J.N., Hampson, R.F., Hynes, R.G., Jenkin, M.E., and Rossi, M. J., Troe, J.: Evaluated kinetic and photochemical data for atmospheric chemistry: volume I - gas phase reactions of O_x, HO_x, NO_x and SO_x species., Atmos. Chem. Phys., 4,1461–1738, https://doi.org/10.5194/acp-4-1461-2004, 2004.

Bougiatioti, A., Nikolaou, P., Stavroulas, I., Kouvarakis, G., Weber, R., Nenes, A., Kanakidou, M., and Mihalopoulos, N.: Particle water and pH in the eastern Mediterranean: source variability and implications for nutrient availability, Atmos. Chem. Phys., 16, 4579–4591, https://doi.org/10.5194/acp-16-4579-2016, 2016.

Chang, Y., Zou, Z., Zhang, Y., Deng, C., Hu, J., Shi, Z., Dore, A. J., and Collett, J. L., Jr.: Assessing contributions of agricultural and nonagricultural emissions to atmospheric ammonia in a Chinese megacity. Environ. Sci. Technol., 53, 1822–1833., https://doi.org/10.1021/acs.est.8b05984, 2019.

Chen, X., Walker, J. T., and Geron, C.: Chromatography related performance of the monitor for aerosols and gases in ambient air (MARGA): laboratory and field-based evaluation. Atmos. Meas. Tech., 10, 3893–3908. https://doi.org/10.5194/amt-10-3893-2017, 2017.

Cheng, Y., Zheng, G., Wei, C., Mu, Q., Zheng, B., Wang, Z., Gao, M., Z., Q., He, K., Carmichael, G., Pöschl, U., and Su, and H.: Reactive nitrogen chemistry in aerosol

water as a source of sulfate during haze events in China, Sci. Adv., 2, e1601530., https://doi.org/10.1126/sciadv.1601530, 2019.

Chow, J. C., Lowenthal, D. H., Chen, L. W. A., Wang, X., and Watson, J. G.: Mass reconstruction methods for $PM_{2.5}$: a review, Air Qual. Atmos. Health., 8, 243 – 263, https://doi.org/10.1007/s11869-015-0338-3, 2015.

Ding, J., Zhao, P., Su, J., Dong, Q., Du, X., and Zhang, Y.: Aerosol pH and its driving factors in Beijing, Atmos. Chem. Phys., 19, 7939–7954., https://doi.org/10.5194/acp-19-7939-2019, 2019.

Ellis, R. A., Murphy, J. G., Markovic, M. Z., VandenBoer, T. C., Makar, P. A., Brook, J., and Mihele, C.: The influence of gas-particle partitioning and surface-atmosphere exchange on ammonia during BAQS-Met, Atmos. Chem. Phys., 11, 133–145., https://doi.org/10.5194/acp-11-133-2011, 2011.

Feng, S., Xu, W., Cheng, M., Ma, Y., Wu, L., Kang, J., Wang, K., Tang, A., Collett, J. L., Fang, Y., Goulding, K., Liu, X., and Zhang, F.: Overlooked nonagricultural and wintertime agricultural NH_3 emissions in Quzhou county, north China plain: evidence from ^{15}N-Stable Isotopes. Environ. Sci. Technol. Lett., 9, 127–133, https://doi.org/10.1021/acs.estlett.1c00935, 2022a.

Feng, T., Zhao, S., Liu, L., Long, X., Gao, C., and Wu, N.: Nitrous acid emission from soil bacteria and related environmental effect over the North China Plain, Chemos., 287, https://doi.org/10.1016/j.chemosphere.2021.132034, 2022b.

Fountoukis, C., Nenes, A.: ISORROPIA II: a computationally efficient thermodynamic equilibrium model for K^+-Ca^{2+}-Mg^{2+}-NH_4^+-Na^+-SO_4^{2-}-NO^{3-}-Cl^--H_2O aerosols. Atmos. Chem. Phys., 7, 4639–4659, https://doi.org/10.5194/acp-7-4639-2007,

2007.

Ge, S., Wang, G., Zhang, S., Li, D., and Zhang, H.: Abundant NH_3 in China enhances atmospheric HONO production by promoting the heterogeneous reaction of SO_2 with NO_2. Environ. Sci. Technol., 53, 14339–14347, https://doi.org/10.1021/acs.est.9b04196, 2019.

Gong, L., Lewicki, R., Griffin, R. J., Flynn, J. H., Lefer, B. L., and Tittel, F. K.: Atmospheric ammonia measurements in Houston, TX using an external-cavity quantum cascade laser-based sensor, Atmos. Chem. Phys., 11, 9721–9733, https://doi.org/10.5194/acp-11-9721-2011, 2011.

Gu, M., Pan, Y., Walters, W. W., Sun, Q., Song, L., Wang, Y., Xue, Y., and Fang, Y.: ehicular emissions enhanced ammonia concentrations in winter mornings: insights from diurnal nitrogen isotopic signatures. Environ. Sci. Technol., 56, 1578–1585, https://doi.org/10.1021/acs.est.1c05884, 2022.

Gunthe, S. S., Rose, D., Su, H., Garland, R. M., Achtert, P., Nowak, A., Wiedensohler, A., Kuwata, M., Takegawa, N., Kondo, Y., Hu, M., Shao, M., Zhu, T., Andreae, M. O., and Pöschl, U.: Cloud condensation nuclei (CCN) from fresh and aged air pollution in the megacity region of Beijing, Atmos. Chem. Phys., 11, 11023–11039, https://doi.org/10.5194/acp-11-11023-2011, 2011.

Han, S., Hong, J., Luo, Q., Xu, H., Tan, H., Wang, Q., Tao, J., Zhou, Y., Peng, L., He, Y., Shi, J., Ma, N., Cheng, Y., and Su, H.: Hygroscopicity of organic compounds as a function of organic functionality, water solubility, molecular weight, and oxidation level, Atmos. Chem. Phys., 22, 3985–4004, https://doi.org/10.5194/acp-22-3985-2022, 2022.

Haskins, J. D., Jaeglé, L., Shah, V., Lee, B. H., Lopez‐Hilfiker, F. D., Campuzano‐Jost, P., Schroder, J. C., Day, D. A., Guo, H., Sullivan, A. P., Weber, R., Dibb, J., Campos, T., Jimenez, J. L., Brown, S. S., and Thornton, J. A.: Wintertime gas‐particle partitioning and speciation of inorganic chlorine in the lower troposphere over the northeast united states and coastal ocean, J. Geophys. Res.: Atmos., 123, https://10.1029/2018jd028786, 2018.

Huang, X., Ding, A., Gao, J., Zheng, B., Zhou, D., Qi, X., Tang, R., Wang, J., Ren, C., Nie, W., Chi, X., Xu, Z., Chen, L., Li, Y., Che, F., Pang, N., Wang, H., Tong, D., Qin, W., Cheng, W., Liu, W., Fu, Q., Liu, B., Chai, F., Davis, S. J., Zhang, Q., and He, K.: Enhanced secondary pollution offset reduction of primary emissions during COVID-19 lockdown in China, Natl. Sci. Rev., 8, nwaa137, https://doi.org/10.1093/nsr/nwaa137, 2021a.

Huang, X., Zhang, J., Zhang, W., Tang, G., and Wang, Y.: Atmospheric ammonia and its effect on $PM_{2.5}$ pollution in urban Chengdu, Sichuan Basin, China. Environ. Pollut., 291, 118–195. https://doi.org/10.1016/j.envpol.2021.118195, 2021b.

Jiang, Y., Xue, L., Shen, H., Dong, C., Xiao, Z., and Wang, W.: Dominant processes of HONO derived from multiple field observations in contrasting environments. Environ. Sci. Technol. Lett., 9, 258–264, https://doi.org/10.1021/acs.estlett.2c00004, 2022.

Kleffmann, J., Gavriloaiei, T., Hofzumahaus, A., Holland, F., Koppmann, R., Rupp, L., Schlosser, E., Siese, M., and Wahner, A.: Daytime formation of nitrous acid: A major source of OH radicals in a forest, Geophys. Res. Lett., 32,

https://doi.org/10.1029/2005gl022524, 2005.

Kramer, L. J., Crilley, L. R., Adams, T. J., Ball, S. M., Pope, F. D., and Bloss, W. J.: Nitrous acid (HONO) emissions under real-world driving conditions from vehicles in a UK road tunnel, Atmos. Chem. Phys., 20, 5231–5248, https://doi.org/10.5194/acp-20-5231-2020, 2020.

Li, J., An, X., Cui, M., Sun, Z., Wang, C., and Li, Y.: Simulation study on regional atmospheric oxidation capacity and precursor sensitivity, Atmos. Environ., 263, 118657, https://doi.org/10.1016/j.atmosenv.2021.118657, 2021a.

Li, S., Song, W., Zhan, H., Zhang, Y., Zhang, X., Li, W., Tong, S., Pei, C., Wang, Y., Chen, Y., Huang, Z., Zhang, R., Zhu, M., Fang, H., Wu, Z., Wang, J., Luo, S., Fu, X., Xiao, S., Huang, X., Zeng, J., Zhang, H., Chen, D., Gligorovski, S., Ge, M., George, C., and Wang, X.: Contribution of vehicle emission and NO_2 surface conversion to nitrous acid (HONO) in urban environments: implications from tests in a tunnel. Environ. Sci. Technol., 55, 15616–15624, https://doi.org/10.1021/acs.est.1c00405, 2021.

Liao, S., Zhang, J., Yu, F., Zhu, M., Liu, J., Ou, J., Dong, H., Sha, Q., Zhong, Z., Xie, Y., Luo, H., Zhang, L., and Zheng, J.: High gaseous nitrous acid (HONO) emissions from light-duty diesel vehicles. Environ. Sci. Technol., 55, 200–208, https://doi.org/10.1021/acs.est.0c05599, 2021.

Liu, J., Deng, H., Lakey, P. S. J., Jiang, H., Mekic, M., Wang, X., Shiraiwa, M., and Gligorovski, S.: Unexpectedly high indoor HONO concentrations associated with photochemical NO_2 transformation on glass windows. Environ. Sci. Technol., 54,

15680–15688, https://doi.org/10.1021/acs.est.0c05624, 2020a.

Liu, M., Song, Y., Zhou, T., Xu, Z., Yan, C., Zheng, M., Wu, Z., Hu, M., Wu, Y., and Zhu, T.: Fine particle pH during severe haze episodes in northern China. Geophys. Res. Lett., 44, 5213–5221, https://doi.org/10.1002/2017gl073210, 2017.

Liu, P., Chen, H., Song, Y., Xue, C., Ye, C., Zhao, X., Zhang, C., Liu, J., and Mu, Y.: Atmospheric ammonia in the rural North China Plain during wintertime: variations, sources, and implications for HONO heterogeneous formation. Sci. Total. Environ., 861, 160768, https://doi.org/10.1016/j.scitotenv.2022.160768, 2023.

Liu, Y., Ni, S., Jiang, T., Xing, S., Zhang, Y., Bao, X., Feng, Z., Fan, X., Zhang, L., and Feng, H.: Influence of Chinese New Year overlapping COVID-19 lockdown on HONO sources in Shijiazhuang, Sci. Total Environ., 745, 141025, https://doi.org/10.1016/j.scitotenv.2020.141025, 2020b.

Liu, Y., Zhang, Y., Lian, C., Yan, C., Feng, Z., Zheng, F., Fan, X., Chen, Y., Wang, W., Chu, B., Wang, Y., Cai, J., Du, W., Daellenbach, K. R., Kangasluoma, J., Bianchi, F., Kujansuu, J., Petäjä, T., Wang, X., Hu, B., Wang, Y., Ge, M., He, H., and Kulmala, M.: The promotion effect of nitrous acid on aerosol formation in wintertime in Beijing: The possible contribution of traffic-related emissions, Atmos. Chem. Phys., 20, 13023–13040, https://doi.org/10.5194/acp-20-13023-2020, 2020c.

Liu, Z., Wang, Y., Costabile, F., Amoroso, A., Zhao, C., Huey, L. G., Stickel, R., Liao, J., and Zhu, T.: Evidence of aerosols as a media for rapid daytime HONO production over China, Environ. Sci. Technol., 48, 13023–13040,

https://doi.org/10.1021/es504163z, 2014.

Lu, K., Guo, S., Tan, Z., Wang, H., Shang, D., Liu, Y., Li, X., Wu, Z., Hu, M., and Zhang, Y.: Exploring atmospheric free-radical chemistry in China: the self-cleansing capacity and the formation of secondary air pollution, Natl. Sci. Rev., 6, 579-594, https://doi.org/10.1093/nsr/nwy073, 2018.

Luo, L., Bai, X., Lv, Y., Liu, S., Guo, Z., Liu, W., Hao, Y., Sun, Y., Hao, J., Zhang, K., Zhao, H., Lin, S., Zhao, S., Xiao, Y., Yang, J., and Tian, H.: Exploring the driving factors of haze events in Beijing during Chinese New Year holidays in 2020 and 2021 under the influence of COVID-19 pandemic, Sci. Total Environ., 859, 160172, https://doi.org/10.1016/j.scitotenv.2022.160172, 2023.

Ma, S.: High-resolution assessment of ammonia emissions in China: Inventories, driving forces and mitigation, Atmos. Environ., 229, https://doi.org/10.1016/j.atmosenv.2020.117458, 2020.

McFall, A. S., Edwards, K. C., and Anastasio, C.: Nitrate photochemistry at the air-ice interface and in other ice reservoirs, Environ. Sci. Technol., 52, 5710–5717, https://doi.org/10.1021/acs.est.8b00095, 2018.

Meng, Z., Xu, X., Lin, W., Ge, B., Xie, Y., Song, B., Jia, S., Zhang, R., Peng, W., Wang, Y., Cheng, H., Yang, W., and Zhao, H.: Role of ambient ammonia in particulate ammonium formation at a rural site in the North China Plain, Atmos. Chem. Phys., 18, 167–184, https://doi.org/10.5194/acp-18-167-2018, 2018.

Meusel, H., Tamm, A., Kuhn, U., Wu, D., Leifke, A. L., Fiedler, S., Ruckteschler, N., Yordanova, P., Lang-Yona, N., Pöhlker, M., Lelieveld, J., Hoffmann, T., Pöschl, U., Su, H., Weber, B., and Cheng, Y.: Emission of nitrous acid from soil and

biological soil crusts represents an important source of HONO in the remote atmosphere in Cyprus, Atmos. Chem. Phys., 18, 799–813, https://doi.org/10.5194/acp-18-799-2018, 2018.

Nah, T., Guo, H., Sullivan, A. P., Chen, Y., Tanner, D. J., Nenes, A., Russell, A., Ng, N. L., Huey, L. G., and Weber, R. J.: Characterization of aerosol composition, aerosol acidity, and organic acid partitioning at an agriculturally intensive rural southeastern US site, Atmos. Chem. Phys., 18, 11471–11491, https://10.5194/acp-18-11471-2018, 2018.

Oswald, R., Behrendt, T., Ermel, M., Wu, D., Su, H., Cheng, Y., Breuninger, C., Moravek, A., Mougin, E., Delon, C., Loubet, B., Pommerening-Roser, A., Sorgel, M., Poschl, U., and Hoffmann, T., Andreae, M.O., Meixner, F.X., Trebs, I.: HONO emissions from soil bacteria as a major source of atmospheric reactive nitrogen., Science, 341, 1233–1235, https://www.science.org/doi/10.1126/science.1242266, 2013.

Pagsberg, P., Bjergbakke, E., Ratajczak, E., Sillesen, A.: Kinetics of the gas phase reaction OH + NO (+M)$^{-}$ > HONO (+M) and the determination of the UV absorption cross sections of HONO., Chem. Phys. Lett., 272, 383–390, https://doi.org/10.1016/s0009-2614(97)00576-9, 1997.

Platt, U., Perner, D., Harris, G. W., Winer, A. M., and Pitts, J. N.: Observations of nitrous acid in an urban atmosphere by differential optical absorption, Nature, 285, 312–314, https://doi.org/10.1038/285312a0, 1980.

Pye, H. O. T., Nenes, A., Alexander, B., Ault, A. P., Barth, M. C., Clegg, S. L., Collett Jr, J. L., Fahey, K. M., Hennigan, C. J., Herrmann, H., Kanakidou, M., Kelly, J. T., Ku, I. T., McNeill, V. F., Riemer, N., Schaefer, T., Shi, G., Tilgner, A., Walker, J.

577 T., Wang, T., Weber, R., Xing, J., Zaveri, R. A., and Zuend, A.: The acidity of
578 atmospheric particles and clouds, Atmos. Chem. Phys., 20, 4809–4888,
579 https://10.5194/acp-20-4809-2020, 2020.
580 Romer, P. S., Wooldridge, P. J., Crounse, J. D., Kim, M. J., Wennberg, P. O., Dibb, J.
581 E., Scheuer, E., Blake, D. R., Meinardi, S., Brosius, A. L., Thames, A. B., Miller,
582 D. O., Brune, W. H., Hall, S. R., Ryerson, T. B., and Cohen, R. C.: Constraints on
583 aerosol nitrate photolysis as a potential source of HONO and NO_x. Environ. Sci.
584 Technol., 52, 13738–13746, https://doi.org/10.1021/acs.est.8b03861, 2018.
585 Scharko, N. K., Berke, A. E., and Raff, J. D.: Release of nitrous acid and nitrogen
586 dioxide from nitrate photolysis in acidic aqueous solutions, Environ. Sci. Technol.,
587 48, 11991–12001, https://doi.org/10.1021/es503088x, 2014.
588 Shi, Q., Tao, Y., Krechmer, J. E., Heald, C. L., Murphy, J. G., Kroll, J. H., and Ye, Q.:
589 Laboratory investigation of renoxification from the photolysis of inorganic
590 particulate nitrate, Environ. Sci. Technol., 55, 854–861,
591 https://doi.org/10.1021/acs.est.0c06049, 2021.
592 Song, S., Gao, M., Xu, W., Shao, J., Shi, G., Wang, S., Wang, Y., Sun, Y., and McElroy,
593 M. B.: Fine-particle pH for Beijing winter haze as inferred from different
594 thermodynamic equilibrium models, Atmos. Chem. Phys., 18, 7423–7438,
595 https://doi.org/10.5194/acp-18-7423-2018, 2018.
596 Song, S., Nenes, A., Gao, M., Zhang, Y., Liu, P., Shao, J., Ye, D., Xu, W., Lei, L., Sun,
597 Y., Liu, B., Wang, S., and McElroy, M. B.: Thermodynamic modeling suggests
598 declines in water uptake and acidity of inorganic aerosols in Beijing winter haze

599 events during 2014/2015–2018/2019. Environ. Sci. Technol. Lett., 6, 752–760,
600 https://doi.org/10.1021/acs.estlett.9b00621, 2019.
601 Spataro, F., and Ianniello, A.: Sources of atmospheric nitrous acid: state of the science,
602 current research needs, and future prospects, J. Air. Waste. Manag. Assoc., 64,
603 1232–1250, https://doi.org/10.1080/10962247.2014.952846, 2014.
604 Stieger, B., Spindler, G., van Pinxteren, D., Grüner, A., Wallasch, M., and Herrmann,
605 H.: Development of an online-coupled MARGA upgrade for the 2 h interval
606 quantification of low-molecular-weight organic acids in the gas and particle phases,
607 Atmos. Meas. Tech. 12, 281–298, https://doi.org/10.5194/amt-12-281-2019, 2019.
608 Su, H., Cheng, Y., Oswald, R., Behrendt, T., Trebs, I., Meixner, F.X., Andreae, M.O.,
609 Cheng, P., and Zhang, Y., Poschl, U.: Soil nitrite as a source of atmospheric HONO
610 and OH radicals., Science., 333, 1616–1618,
611 https://doi.org/10.1126/science.1207687, 2011.
612 Twigg, M. M., Berkhout, A. J. C., Cowan, N., Crunaire, S., Dammers, E., Ebert, V.,
613 Gaudion, V., Haaima, M., Häni, C., John, L., Jones, M. R., Kamps, B., Kentisbeer,
614 J., Kupper, T., Leeson, S. R., Leuenberger, D., Lüttschwager, N. O. B., Makkonen,
615 U., Martin, N. A., Missler, D., Mounsor, D., Neftel, A., Nelson, C., Nemitz, E.,
616 Oudwater, R., Pascale, C., Petit, J.-E., Pogany, A., Redon, N., Sintermann, J.,
617 Stephens, A., Sutton, M. A., Tang, Y. S., Zijlmans, R., Braban, C. F., and
618 Niederhauser, B.: Intercomparison of in situ measurements of ambient NH_3:
619 instrument performance and application under field conditions, Atmos. Meas.
620 Tech., 15, 6755–6787, https://doi.org/10.5194/amt-15-6755-2022, 2022.

Wang, C., Yin, S., Bai, L., Zhang, X., Gu, X., Zhang, H., Lu, Q., and Zhang, R.: High-resolution ammonia emission inventories with comprehensive analysis and evaluation in Henan, China, 2006–2016, Atmos. Environ., 193, 11–23, https://doi.org/10.1016/j.atmosenv.2018.08.063, 2018.

Wang, S., Wang, L., Li, Y., Wang, C., Wang, W., Yin, S., and Zhang, R.: Effect of ammonia on fine-particle pH in agricultural regions of China: comparison between urban and rural sites, Atmos. Chem. Phys., 20, 2719–2734, https://doi.org/10.5194/acp-20-2719-2020, 2020.

Wang, S., Wang, L., Fan, X., Wang, N., Ma, S., and Zhang, R.: Formation pathway of secondary inorganic aerosol and its influencing factors in Northern China: Comparison between urban and rural sites, Sci. Total Environ., 840, https://doi.org/10.1016/j.scitotenv.2022.156404, 2022.

Wang, S., Fan, X., Xu, Y., Zhang, R., and Ren, B.: Insight into the non-linear responses of particulate sulfate to reduced SO_2 concentration: A perspective from the aqueous-phase reactions in a megacity in Northern China, Atmos. Res., 290, https://doi.org/10.1016/j.atmosres.2023.106796, 2023a.

Wang, W., Wang, S., Xu, J., Zhou, R., Shi, C., and Zhou, B.: Gas-phase ammonia and $PM_{2.5}$ ammonium in a busy traffic area of Nanjing, China, Environ. Sci. Pollut. Res. Int., 23, 1691–1702, https://doi.org/10.1007/s11356-015-5397-3, 2016.

Wang, Y., Jin, X., Liu, Z., Wang, G., Tang, G., Lu, K., Hu, B., Wang, S., Li, G., An, X., Wang, C., Hu, Q., He, L., Zhang, F., and Zhang, Y.: Progress in quantitative research on the relationship between atmospheric oxidation and air quality, J.

643 Environ. Sci., 123, 350–366, https://doi.org/10.1016/j.jes.2022.06.029, 2023b.
644 Wells, M., Choularton, T. W., and Bower, K. N.: A modelling study of the interaction
645 of ammonia with cloud., Atmos. Environ., 32, 359–363,
646 https://doi.org/10.1016/s1352-2310(97)00199-4, 1998.
647 Wentworth, G. R., Murphy, J. G., Benedict, K. B., Bangs, E. J., and Collett Jr, J. L.: The
648 role of dew as a night-time reservoir and morning source for atmospheric ammonia,
649 Atmos. Chem. Phys., 16, 7435–7449, https://doi.org/10.5194/acp-16-7435-2016,
650 2016.
651 Wu, C., Lv, S., Wang, F., Liu, X., Li, J., Liu, L., Zhang, S., Du, W., Liu, S., Zhang, F.,
652 Li, J., Meng, J., and Wang, G.: Ammonia in urban atmosphere can be substantially
653 reduced by vehicle emission control: A case study in Shanghai, China, J. Environ.
654 Sci., 126, 754–760, https://doi.org/10.1016/j.jes.2022.04.043, 2023.
655 Xie, Y., Wang, G., Wang, X., Chen, J., Chen, Y., Tang, G., Wang, L., Ge, S., Xue, G.,
656 Wang, Y., and Gao, J.: Nitrate-dominated $PM_{2.5}$ and elevation of particle pH
657 observed in urban Beijing during the winter of 2017. Atmos. Chem. Phys., 20,
658 5019–5033, https://doi.org/10.5194/acp-20-5019-2020, 2020.
659 Xing, L., Fu, T. M., Cao, J. J., Lee, S. C., Wang, G. H., Ho, K. F., Cheng, M. C., You,
660 C. F., and Wang, T. J.: Seasonal and spatial variability of the OM/OC mass ratios
661 and high regional correlation between oxalic acid and zinc in Chinese urban
662 organic aerosols, Atmos. Chem. Phys., 13, 4307–4318,
663 https://doi.org/10.5194/acp-13-4307-2013, 2013.
664 Xu, J., Chen, J., Zhao, N., Wang, G., Yu, G., Li, H., Huo, J., Lin, Y., Fu, Q., Guo, H.,

665 Deng, C., Lee, S.-H., Chen, J., and Huang, K.: Importance of gas-particle
666 partitioning of ammonia in haze formation in the rural agricultural environment,
667 Atmos. Chem. Phys., 20, 7259–7269, https://doi.org/10.5194/acp-20-7259-2020,
668 2020.
669 Xu, W., Kuang, Y., Zhao, C., Tao, J., Zhao, G., Bian, Y., Yang, W., Yu, Y., Shen, C.,
670 Liang, L., Zhang, G., Lin, W., and Xu, X.: NH_3-promoted hydrolysis of NO_2
671 induces explosive growth in HONO, Atmos. Chem. Phys., 19, 10557–10570,
672 https://doi.org/10.5194/acp-19-10557-2019, 2019.
673 Xu, W., Zhao, Y., Wen, Z., Chang, Y., Pan, Y., Sun, Y., Ma, X., Sha, Z., Li, Z., Kang, J.,
674 Liu, L., Tang, A., Wang, K., Zhang, Y., Guo, Y., Zhang, L., Sheng, L., Zhang, X.,
675 Gu, B., Song, Y., Van Damme, M., Clarisse, L., Coheur, P. F., Collett, J. L., Jr.,
676 Goulding, K., Zhang, F., He, K., and Liu, X.: Increasing importance of ammonia
677 emission abatement in $PM_{2.5}$ pollution control. Sci. Bull., 67, 1745–1749,
678 https://doi.org/10.1016/j.scib.2022.07.021, 2022.
679 Xue, C.: Substantially growing interest in the chemistry of nitrous acid (HONO) in
680 China: current achievements, problems, and future directions. Environ. Sci.
681 Technol., 56, 7375–7377. https://doi.org/10.1021/acs.est.2c02237, 2022.
682 Ye, C., Zhang, N., Gao, H., and Zhou, X.: Photolysis of particulate nitrate as a source
683 of HONO and NO_x. Environ. Sci. Technol., 51, 6849–6856,
684 https://doi.org/10.1021/acs.est.7b00387, 2017.
685 Ye, X., Ma, Z., Zhang, J., Du, H., Chen, J., Chen, H., Yang, X., Gao, W., and Geng, F.:
686 Important role of ammonia on haze formation in Shanghai, Environ. Res. Lett., 6,

024019, https://doi.org/10.1088/1748-9326/6/2/024019, 2011.

Zhang, Q., Liu, P., Wang, Y., Gerorge, C., Chen, T., Ma, S. L., Ren, Y., Mu, Y., Song, M., Herrmann, H., Mellouki, A., Chen, J., Zhao, X., Wang, S., and Y., Z.: Unveiling the underestimated direct emissions of nitrous acid (HONO), Proc. Natl. Acad. Sci. U.S.A., 120, https://doi.org/10.1073/pnas.2302048120, 2023.

Zhang, W., Tong, S., Jia, C., Wang, L., Liu, B., Tang, G., Ji, D., Hu, B., Liu, Z., Li, W., Wang, Z., Liu, Y., Wang, Y., and Ge, M.: Different HONO sources for three layers at the urban area of Beijing. Environ. Sci. Technol., 54, 12870–12880, https://doi.org/10.1021/acs.est.0c02146, 2020a.

Zhang, W., Tong, S., Jia, C., Ge, M., Ji, D., Zhang, C., Liu, P., Zhao, X., Mu, Y., Hu, B., Wang, L., Tang, G., Li, X., Li, W., and Wang, Z.: Effect of different combustion processes on atmospheric nitrous acid formation mechanisms: a winter comparative observation in urban, suburban and rural areas of the North China Plain. Environ. Sci. Technol., 56, 4828–4837, https://doi.org/10.1021/acs.est.1c07784, 2022.

Zhang, Y., Liu, X., Fang, Y., Liu, D., Tang, A., and Collett, J. L.: Atmospheric ammonia in Beijing during the COVID-19 outbreak: concentrations, sources, and implications. Environ. Sci. Technol. Lett., 8, 32–38, https://doi.org/10.1021/acs.estlett.0c00756, 2020b.

Figures:

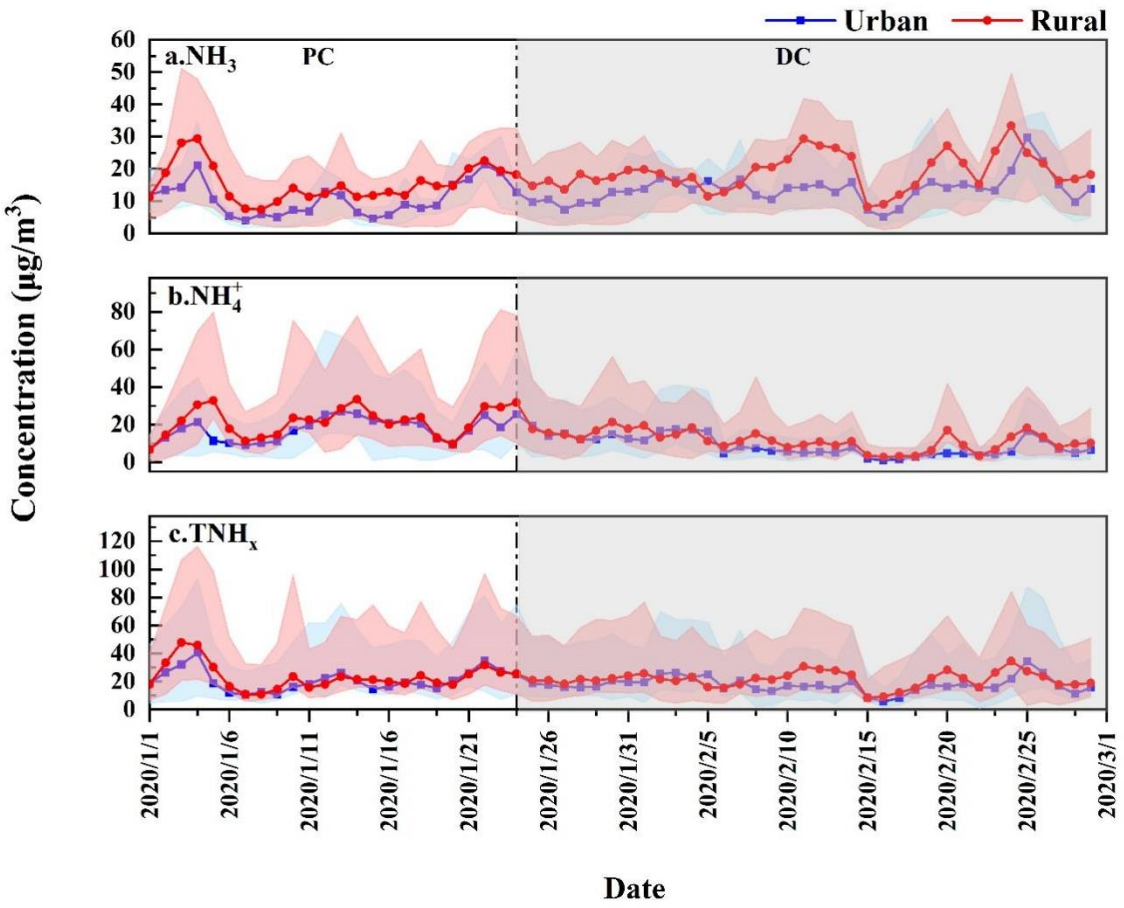

Figure 1. Temporal variations of a. NH_3, b. NH_4^+, and c. TNH_x at the urban and rural sites before (PC) and during (DC) the COVID-19 outbreak, respectively. The shaded areas of the curve represent the maximum and minimum values.

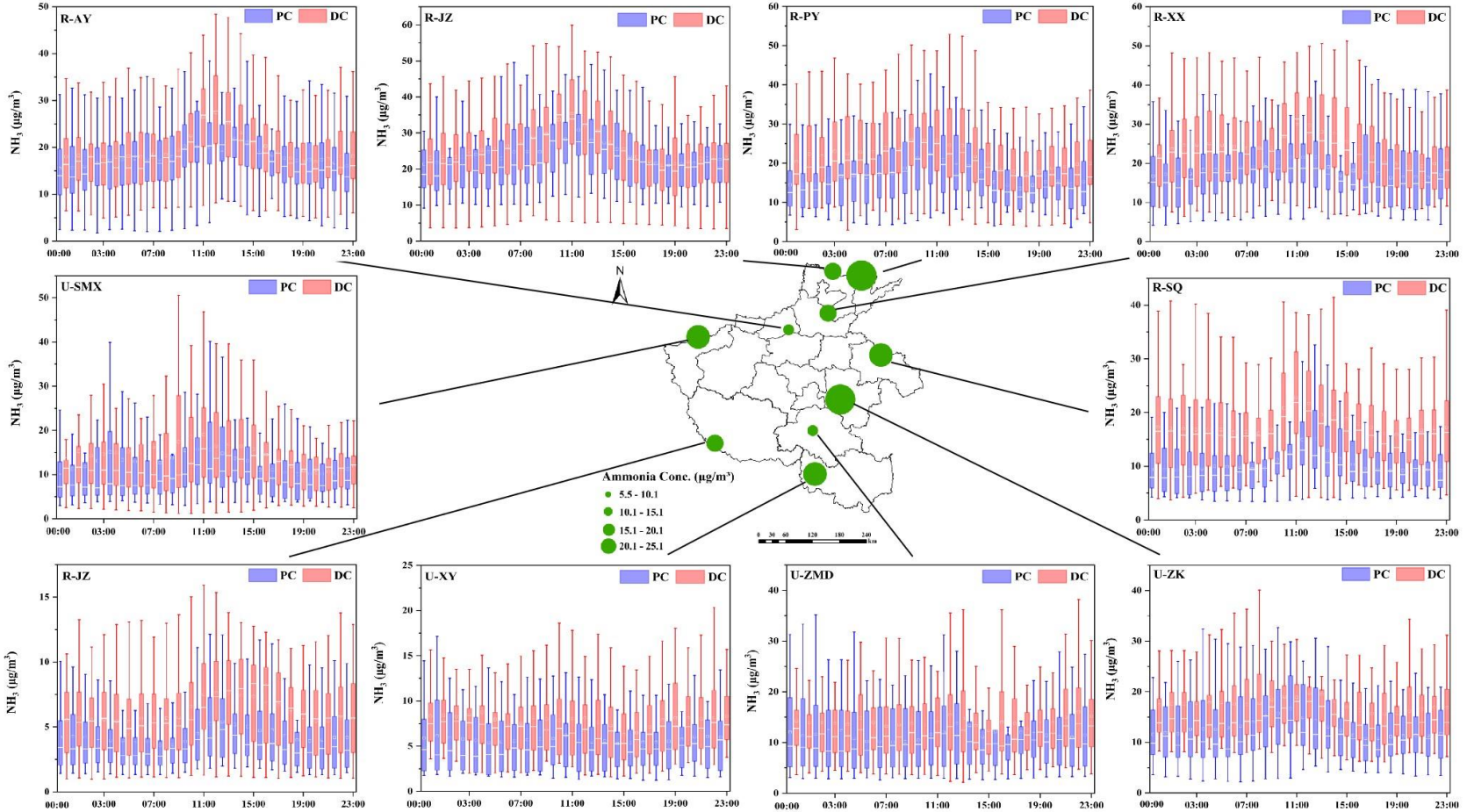

Figure 2. Daily variation of NH_3 concentrations at ten sites before (PC) and during (DC) the COVID-19 outbreak. The green dots represent the location of ten sites and their size represents the concentration of NH_3; In each box, the top, middle, and bottom lines represent the 75, 50, and 25 percentiles of statistical data, respectively; the upper and lower whiskers represent the 90 and 10 percentiles of statistical data, respectively.

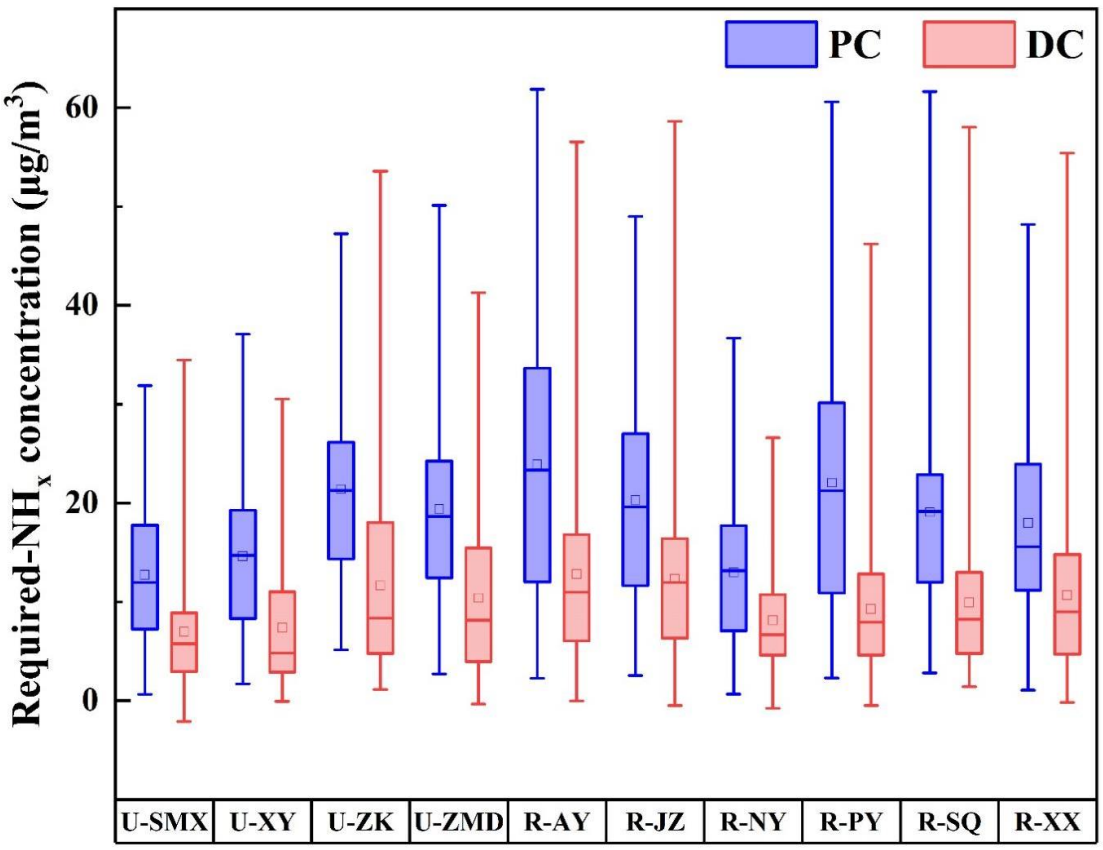

715

716 Figure 3. Box diagram of changes in Required-NH_x at ten sites before (PC) and during

717 (DC) the COVID-19 outbreak. In each box, the top, middle, and bottom lines represent

718 the 75, 50, and 25 percentiles of statistical data, respectively; the upper and lower

719 whiskers represent the 90 and 10 percentiles of statistical data, respectively.

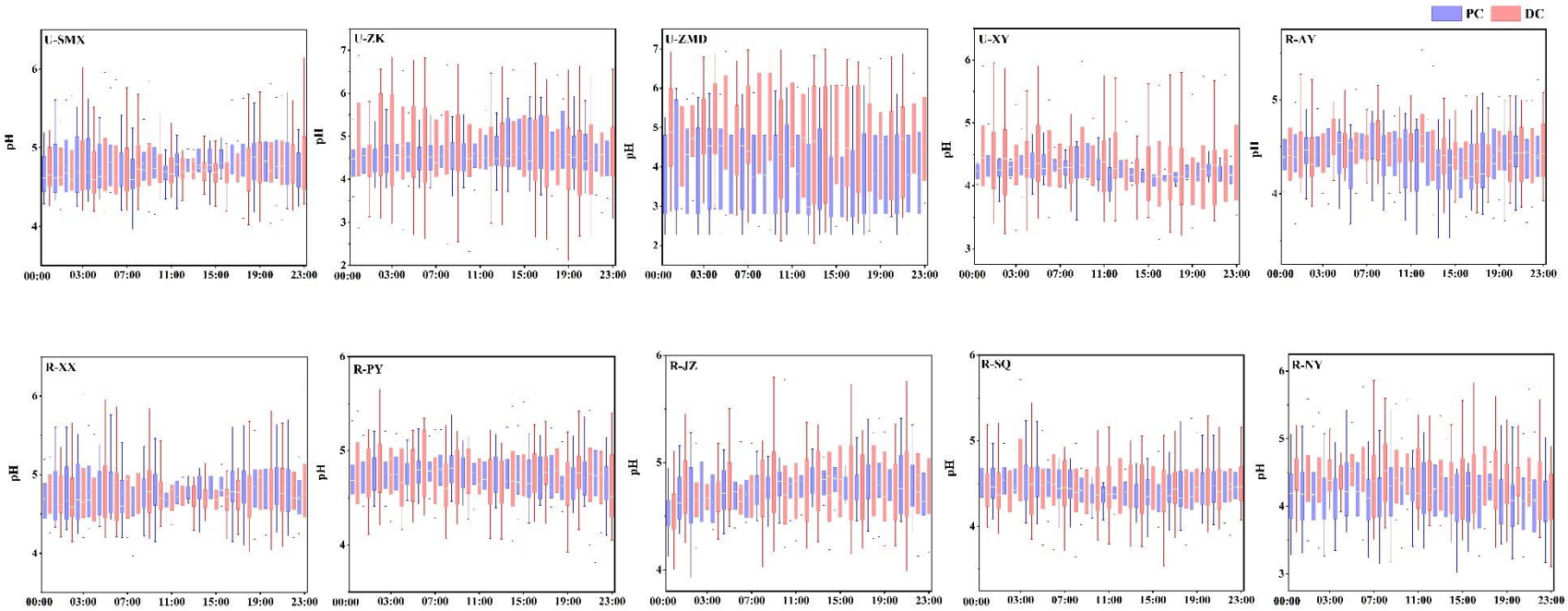

720

721 Figure 4. Diurnal patterns of pH at ten sites before (PC) and during (DC) the COVID-19 outbreak. In each box, the top, middle, and bottom

722 lines represent the 75, 50, and 25 percentiles of statistical data, respectively; the upper and lower whiskers represent the 90 and 10 percentiles of

723 statistical data, respectively.

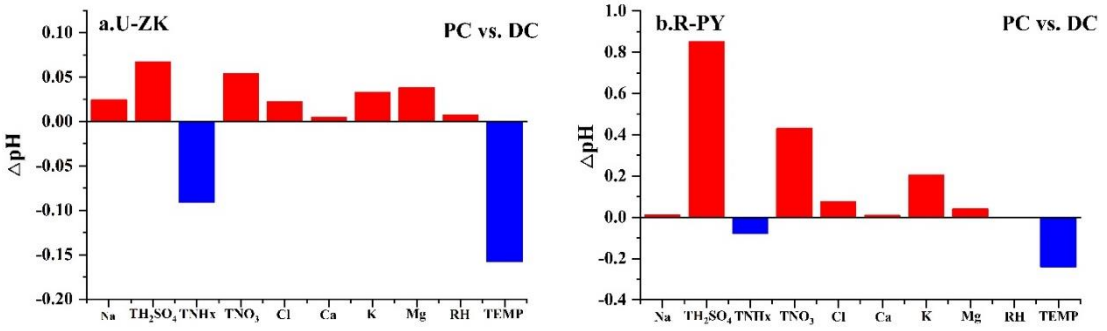

724

725 Figure 5. Changes of pH (ΔpH) through the sensitivity tests (Figure S5 and S6) by

726 changing parameters between PC and DC at the a. U-ZK and b. R-PY sites.

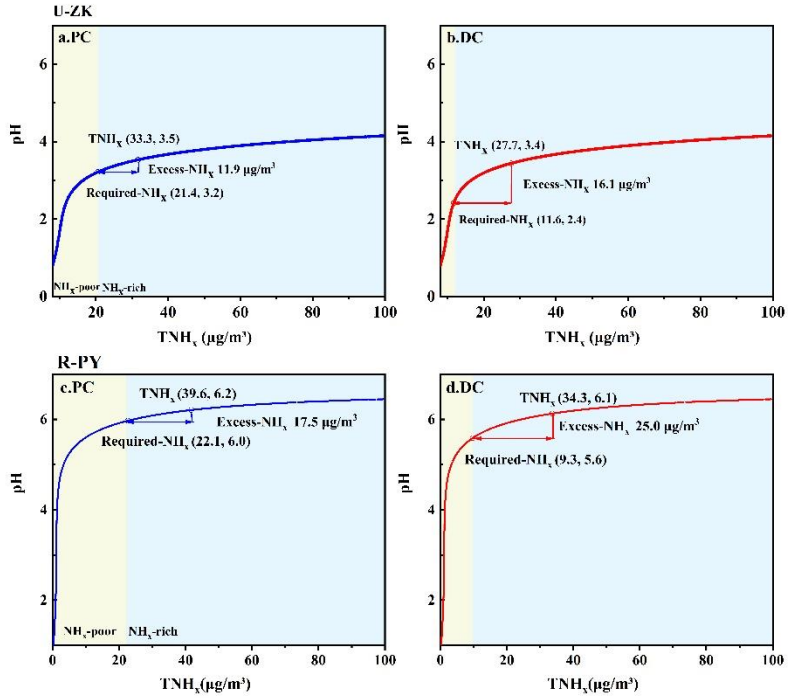

727

728 Figure 6. Particle pH corresponds to increasing TNH_x at U-ZK and R-PY sites to

729 examine the effects of major indicators of NH_3 (i.e., TNH_x, Required-NH_x, and Excess-

730 NH_x) on aerosol acidity. Particle pH was calculated by using a wide range of TNH_x

731 (25–130 μg/m^3) and average values of other parameters in PC and DC of U-ZK and R-

732 PY sites. The concentrations of TNH_x, Required-NH_x, and Excess-NH_x with

733 corresponding pH values are marked by a hollow box, hollow circle, and arrow

734 respectively. The yellow and blue background colors correspond to the NH_x-poor and

735 NH_x-rich, respectively.

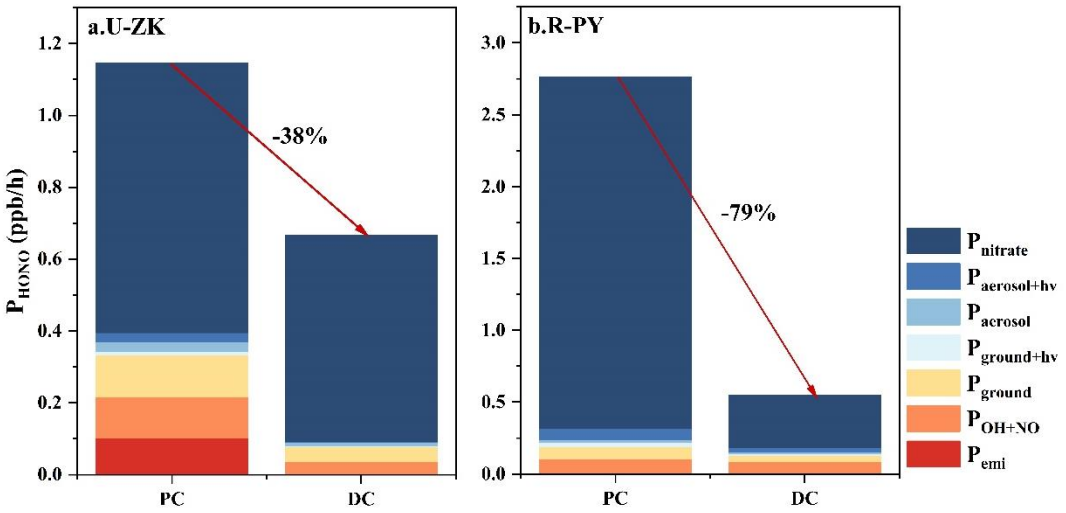

Figure 7. Comparison of HONO sources at a. U-ZK and b. R-PY sites before (PC) and during (DC) the COVID-19 outbreak. The calculation method can be found in Text S4.

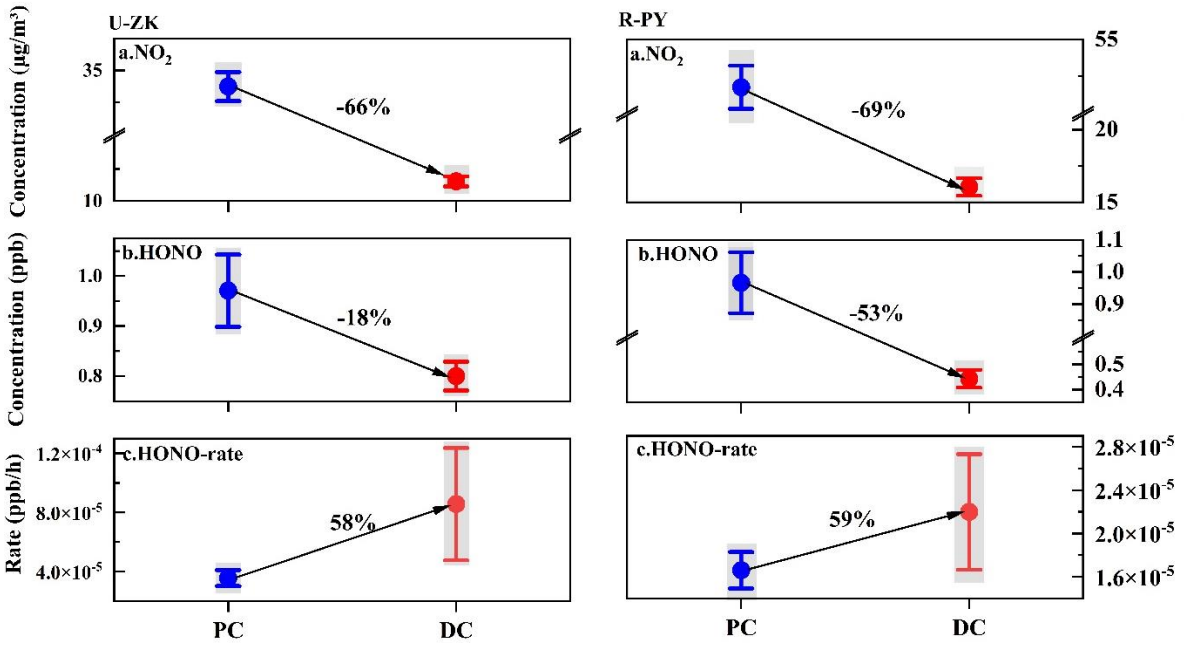

Figure 8. Decline ratios of a. NO_2, b. HONO concentration, and c. HONO production rate at U-ZK and R-PY sites before (PC) and during (DC) the COVID-19 outbreak. The center point represents the mean value, and the upper and lower whiskers represent the 95% confidence interval of the mean. The shadows in the figure represent the uncertainties of NO_2 measurement (±10%), HONO measurement (±20%), and the

746 HONO formation rate of R_1 reaction (–78–123%), respectively.

747

748 **Table:**

749 Table 1. Changes in concentrations (mean ± standard deviation) of NH_3, NH_4^+, and
750 TNH_x at ten sites during entire periods (Average), before (PC), and during (DC) the
751 COVID-19 outbreak.

Sites	Substances	Average (μg/m³)	PC (μg/m³)	DC (μg/m³)
U-SMX	NH_3	13.8 ± 10.8	12.6 ± 10.1	14.5 ± 11.1
	NH_4^+	10.9 ± 7.2	14.2 ± 7.2	8.8 ± 6.5
	TNH_x	22.9 ± 14.1	24.9 ± 14.5	21.7 ± 13.8
U-ZK	NH_3	15.6 ± 8.3	12.7 ± 6.5	17.4 ± 8.8
	NH_4^+	13.6 ± 9.3	19.1 ± 8.4	10.3 ± 8.1
	TNH_x	28.6 ± 13.7	30.9 ± 12.8	27.1 ± 14.0
U-ZMD	NH_3	13.1 ± 8.4	11.6 ± 8.2	14.0 ± 8.4
	NH_4^+	13.9 ± 9.8	19.6 ± 10.3	10.3 ± 7.5
	TNH_x	25.7 ± 14.6	30.3 ± 15.1	22.8 ± 13.5
U-XY	NH_3	7.0 ± 4.3	5.7 ± 4.0	7.9 ± 4.3
	NH_4^+	11.0 ± 7.7	15.4 ± 7.6	8.3 ± 6.5
	TNH_x	17.6 ± 9.8	20.6 ± 10.1	15.7 ± 9.2
R-AY	NH_3	19.0 ± 8.4	17.9 ± 8.3	19.7 ± 8.4
	NH_4^+	19.3 ± 12.9	26.4 ± 13.7	15.0 ± 10.3
	TNH_x	36.6 ± 18.2	41.7 ± 20.4	33.4 ± 16.0
R-XX	NH_3	21.7 ± 10.2	18.1 ± 9.3	23.8 ± 10.1
	NH_4^+	15.9 ± 10.4	20.6 ± 11.0	13.0 ± 8.8
	TNH_x	34.9 ± 17.0	35.1 ± 18.8	34.8 ± 15.8
R-PY	NH_3	19.8 ± 9.4	16.8 ± 8.1	21.7 ± 9.6
	NH_4^+	17.4 ± 11.8	25.3 ± 12.6	12.4 ± 8.0
	TNH_x	35.2 ± 17.8	39.4 ± 19.8	32.6 ± 15.7
R-JZ	NH_3	25.3 ± 11.5	24.1 ± 11.5	25.9 ± 11.4
	NH_4^+	17.3 ± 11.3	22.7 ± 11.6	14.2 ± 9.9
	TNH_x	40.8 ± 20.1	42.9 ± 22.8	33.5 ± 18.2
R-SQ	NH_3	15.0 ± 7.9	10.3 ± 5.2	17.7 ± 7.9
	NH_4^+	13.4 ± 8.5	18.9 ± 8.6	10.3 ± 6.7
	TNH_x	26.3 ± 13.2	25.5 ± 14.0	26.8 ± 12.7
R-NY	NH_3	5.5 ± 3.1	4.3 ± 2.7	6.2 ± 3.2
	NH_4^+	10.2 ± 6.9	13.3 ± 7.2	8.4 ± 6.1
	TNH_x	14.8 ± 8.5	16.0 ± 9.5	14.1 ± 7.8

752

753